Sustainable Energy & Fuels

Modeling Electrochemical Behavior and Interfacial Junction Profiles of Bipolar Membranes at Solar Flux Relevant Operating Current Densities

Journal:	*Sustainable Energy & Fuels*
Manuscript ID	SE-ART-02-2021-000201
Article Type:	Paper
Date Submitted by the Author:	09-Feb-2021
Complete List of Authors:	Lin, Meng; Southern University of Science and Technology, Department of Mechanical and Energy Engineering Digdaya, Ibadillah A.; California Institute of Technology Xiang, Chengxiang; California Institute of Technology,

Modeling Electrochemical Behavior and Interfacial Junction Profiles of Bipolar Membranes at Solar Flux Relevant Operating Current Densities

Meng Lin[a], Ibadillah A. Digdaya[b], Chengxiang Xiang[b*]*

[a] Department of Mechanical and Energy Engineering, Southern University of Science and Technology, Shenzhen 518055, China

[b]Liquid Sunlight Alliance, and Division of Engineering and Applied Science, California Institute of Technology, Pasadena, California 91125, United States

[c]Division of Chemistry and Chemical Engineering, California Institute of Technology, Pasadena, CA 91125, USA

*To whom correspondence should be addressed: cxx@caltech.edu, linm@sustech.edu.cn

ABSTRACT

A 1-dimensional, multi-physics model that accounts for migration and diffusion of solution species, electrostatics, chemical reactions, in particular water dissociation (WD) at the bipolar membrane (BPM) interface was developed to study the electrochemical behavior of bipolar membrane (BPM) at solar flux relevant operating current densities (tens of mA cm^{-2}). Significant partial current densities for WD were observed at BPM voltages much less than the equilibrium voltage, e.g., *59* mV×ΔpH from both from experiments and from the modeling. The co-ion leaking across the BPM at pH differentials accounted for the early presence of the partial current density for WD. Two distinctive electric field dependent WD pathways, the un-catalyzed pathway and the catalyzed pathway, were simulated quantitatively and parametrically studied to improve the turn-on potential of the BPM. The catalyzed pathway accounted for the majority of the partial current density for WD at low voltages, while the un-catalyzed pathway dominated the WD at relatively high voltages. Significant WD was observed only within the interfacial CL (<5 nm), in which large electric field was present. To improve the electrochemical behavior and the turn-on potential of BPM, the impacts of the pKa of the immobilized WD catalysts, the electric-field dependent rate constant, as well as the thickness of the catalyst layer and the fixed charge density in BPM on the partial current densities for WD was studied systematically. In addition, the electrochemical behavior and concentration profiles of BPM under buffered electrolyte was studied and contrasted with un-buffered electrolyte from both modeling and experiments.

Introduction

Bipolar membrane (BPM) has been used in many device configurations in solar fuel applications, including solar-driven water-splitting cells[1,2] and solar-driven CO_2 reduction (CO_2R) cells.[3–5] The use of BPM in solar-fuel devices can achieve many unique operating conditions that cannot be obtained by using cation exchange membrane (CEM) or anion exchange membrane alone. First of all, BPM can sustain pH differentials between the catholyte and anolyte and hence offered unique opportunities to different electrolyte combinations for more efficient and stable solar fuel devices.[6] Secondly, the use of both CEM and AEM can effectively block the crossover of bicarbonate ions between the catholyte and anolyte, which was the main origin for CO_2 loss in aqueous based electrochemical cells for CO_2R.[7,8] In addition, BPM based electrochemical cell configurations that leveraged the local acidification of electrolyte and local generation of CO_2 have shown promises in bicarbonate/carbonate feed CO_2R devices.[9,10] While BPMs are widely used in electrodialysis and electrolysis applications,[11–13] the operating current densities as well as the electrolyte combinations are quite different from solar fuel applications, e.g., the operating current density in electrolysis or electrodialysis systems are often a couple orders of magnitude higher than in the solar fuel devices. In addition, most electrolysis and electrodialysis systems leverages the low transport loss and high water dissociation rates of BPM at high pH differentials, e.g., pH=0/pH=14, and the BPM resistive loss accounts for the majority of the voltage loss in the system. In comparison, solar fuel devices, in particular for CO_2R, rarely operate at extreme pHs due to catalyst selectivity, and often required to minimize the pH gradients and the concentration overpotential related to fuel forming reactions.[14,15] As a result, large voltage losses were observed experimentally in various electrolyte combinations even at relatively low operating current density in the range of tens of mA cm^{-2}.[16,17] As a result, large voltage losses were observed experimentally

in various electrolyte combinations even at relatively low operating current density in the range of tens of mA cm^{-2}.[16,17]

The operating principle of BPM was often compared and contrasted with solid-state semiconductor p-n junctions.[18] However, the electric-field dependent WD kinetics[19] and impacts of WD catalysts at the reverse bias[20] was often not considered. Recent report showed that at high operating current densities (>100 mA cm^{-2}), the WD catalysts played a governing role in relative to the electric field at the interface, and BPMs with engineered 3D junctions exhibited lower potential drops.[21] In addition, the inclusion of WD catalyst materials with different point of zero charge at the BPM interface has shown significant impact on the overall current voltage characteristics in a water-feed electrolysis cell without any co-ions.[22] The dissociation of weak electrolytes under an applied electric field was studied by Onsager[23] and an analytical expression was obtained without the consideration of the length of the chemical bond in the paired ions. The improved model developed by Craig indicates that the WD rates can be varied by many orders of magnitude with small changes in the length of the chemical bond.[24] In this study, the electrochemical behavior of BPM as well as the potential and net charge profiles at the BPM interface in both un-buffered electrolytes and buffered electrolytes were modeled and studied by a 1-D Multiphysics model that accounted for migration and diffusion of solutions species, electrostatics and chemical reactions, in particular the WD kinetics using the improved model by Craig and others.[21,24,25] The effects of the WD kinetics, the thickness of the catalyst layer and the fixed charge densities on the voltage across the BPM at current densities that are relevant to solar fuel devices were modeled and simulated.

Physical-based model development

Figure 1a shows a schematic illustration of the modeling domain for the BPM. The simulation domain includes, a CEM layer (CEL), a catalyst layer (CL), an AEM layer (AEL), and two electrolyte boundary layers (BL) at each side of BPM. For electrolyte with extreme pH differentials (pH=0/pH=14), 1 M HCl and 1 M KOH were used, while for electrolyte at the same pH (pH=7/pH=7), 0.5 M K_2SO_4 was used at both sides of the BPM. The thickness of CEL and AEL layers were set to 75 μm. The thickness of the CL was set to 10 nm for the reference case.[24] The BL thickness was set to 50 μm to account for moderate stirring or recirculation in the cell.

Two pathways of water disassociation (i.e., the un-catalyzed pathway and the catalyzed pathway) were included in this study. The electric field dependent, un-catalyzed water disassociation reaction (R1) was modeled across the whole simulation domain:

$$2H_2O \overset{k^E_{+1}, k^E_{-1}}{\Longleftrightarrow} H_3O^+ + OH^- \qquad (1, R1)$$

where $k^E_{+1} = f_{E,\,enhance,\,f} k^0_{+1}$ and $k^E_{-1} = f_{E,\,enhance,\,b} k^0_{-1}$ are the forward and backward reaction rate constants.

The equilibrium constant of the un-catalyzed pathway was defined as

$$K^E_1 = \frac{k^E_{+1}}{k^E_{-1}} = \frac{c_{H_3O} + c_{OH^-}}{c^2_{H_2O}} \qquad (2)$$

The equilibrium constant of the un-catalyzed pathway at zero electric field was defined as

$$K^0_1 = \frac{k^0_{+1}}{k^0_{-1}}. \qquad (3)$$

The intrinsic reaction rate constants (i.e., k^0_{+1} and k^0_{-1}) were set to 3.67×10^{-10} $m^3 s^{-1} mol^{-1}$ and 1.11×10^8 $m^3 s^{-1} mol^{-1}$ based on the analytical correlation proposed by Craig.[24] As a result,

$K_1^0 = \frac{k_{+1}^0}{k_{-1}^0} = 3.3 \times 10^{-18}$. Considering a bulk water concentration of 55.34 M, $c_{H_3O^+} c_{OH^-}$ gives 10^{-14} M^2 at zero electric field. As a result, pKa + pKb =14 for water dissociation reaction (Eq. 1) at zero electric field.

The enhancement factor of forward reaction ($f_{E,\text{ enhance, f}}$) and back forward reaction ($f_{E,\text{ enhance, b}}$) based on the extended Onsager method for chemical bonds with empirical fitting were given as[24]

$$f_{E,\text{ enhance, f}} = \left(\sum_{n=0}^{\infty} \frac{(2\underline{\underline{E}}_d)^n}{n!(n+1)!}\right) cosh\,(\tau \underline{\underline{E}}_d)(cosh\,(\tau))^{\underline{\underline{E}}_d} \quad (4)$$

$$f_{E,\text{ enhance, b}} = 1 + \frac{1 - exp\left(-\frac{1}{\alpha}\right)}{2}\left(\alpha^2 \underline{\underline{E}}_d + 4.97\alpha \frac{sinh\,(0.0835\alpha \underline{\underline{E}}_d)}{cosh\,(0.0835\alpha \underline{\underline{E}}_d)^2}\right) \quad (5)$$

where $\tau = 0.128\ln(\cos(0.235\alpha)) + 5.72\alpha^2$ is a fitting parameter with $\alpha = \frac{7.28\varepsilon_{H_2O} RT}{eF}$, $E_d = \frac{0.29}{\alpha}$ $\left|\frac{eE}{k_B T}\right|$ is the dimensionless electric field. It is important to note that with the presence of an electric field, $c_{H_3O^+} c_{OH^-}$ no longer equals to a constant (10^{-14} M^2). The product of the hydronium concentration and the hydroxide concentration during active WD reactions under the electric field was given by:

$$c_{H_3O^+} c_{OH^-} = 10^{-14}\ M^2 \times f_{E,\text{ enhance, f}} / f_{E,\text{ enhance, b}} \quad (6)$$

When the simulation reached steady state, in which the concentrations of all species stopping changing, the generation rate of hydronium and hydroxide ion equal to their recombination rate, which yielded Eq. 6. The catalyzed pathway included two sequential chemical reactions, Eq. 7 and Eq. 9 (Noted as R2 and R3). The first chemical reaction, Eq. 7, was the WD reaction in the presence of a WD catalyst (noted as C_{WD}) or the protonation of the WD catalyst, and the second chemical reaction, Eq.9, was the deprotonation of the WD catalyst. The first chemical reaction has the same electric-field dependent WD enhancement factors, $f_{E,\text{ enhance, f}}$ and $f_{E,\text{ enhance, b}}$, as the un-

catalyzed pathway, while the equilibrium constant at zero electric field was significantly higher than the un-catalyzed WD pathway. The second chemical reaction was assumed to be electric-field independent because no net production of charges took place in Eq. 7.[24]

$$H_2O + C_{WD} \overset{k_{+2}^E, k_{-2}^E}{\Longleftrightarrow} C_{WD}H^+ + OH^- \quad (7, R2)$$

$$\frac{k_{+2}^E}{k_{-2}^E} = \frac{c_{C_{WD}H^+}\, c_{OH^-}}{c_{C_{WD}} c_{H_2O}} \quad (8)$$

$$H_2O + C_{WD}H^+ \overset{k_{+3}, k_{-3}}{\Longleftrightarrow} H_3O^+ + C_{WD} \quad (9, R3)$$

$$\frac{k_{+3}^E}{k_{-3}^E} = \frac{c_{C_{WD}} c_{H_3O^+}}{c_{C_{WD}H^+} c_{H_2O}} \quad (10)$$

The intrinsic reaction rate constants for R2 and R3 were set as the following: k_{+2}^0= 83.9 $m^3 s^{-1} mol^{-1}$,$k_{-2}^0 = 2.13 \times 10^7\ m^3 s^{-1} mol^{-1}$, k_{+3}^0= $1.8 \times 10^{-5}\ m^3 s^{-1} mol^{-1}$,$k_{-3}^0 = 2.15 \times 10^7\ m^3 s^{-1} mol^{-1}$.[24] The reaction rates for R2 were also dependent on electric field due to net charge generation in the reaction. The reaction enhance factor for R2 followed the same relation as R1 (Eqs. 4 and 5). In this study, the concentration of the total concentration of catalyst ($C_{WD} + C_{WD}H^+$) was set to 1.0 M (equals to the fixed charge concentration for BPM) over the 10 nm CL. It is important to note that the catalyzed pathway and un-catalyzed pathway are not thermodynamically independent; from Eqs. 3, 8 and 10, the general rate relation follows:

$$\frac{k_{+3}^E k_{+2}^E}{k_{-3}^E k_{-2}^E} = \frac{k_{+1}^E}{k_{-1}^E} \quad (11)$$

For the cases with buffer solution, the phosphate buffer reaction (R4) in the electrolyte was estimated based on its pKa (6.62 at 1.0 M)[26]

$$H_2O + H_2PO_4^- \overset{k_{+4}, k_{-4}}{\Longleftrightarrow} HPO_4^{2-} + H_3O^+ \quad (12, R4)$$

where k_{+4} and k_{-4} was set to 10^2 s^{-1} and 4.17×10^3 m^{3}s^{-1}mol^{-1}, respectively. The protonation and deprotonation of the buffer species were sufficiently fast, the simulation results were only dependent of the pKa of the buffer and were not dependent on k_{+4} and k_{-4} used in the study. In addition to the WD reactions, homogeneous reactions due to ion-pairing (R5) were also considered as the following:

$$KSO_4^- \overset{k_{+5},k_{-5}}{\Longleftrightarrow} SO_4^{2-} + K^+ \quad (13, R5)$$

Note that R5 was only considered for the un-buffered electrolyte with K_2SO_4 electrolyte. The equilibrium constant for ion pairing (K_5) for R5 at 25 °C was set to 0.483 M,[27] where k_{+5} and k_{-5} were set to 10^2 s^{-1} and 0.21 m^{3}s^{-1}mol^{-1}, respectively. Full disassociation was assumed for HCl and KOH electrolytes at the extreme pH differential (pH=0/pH=14).

The Nernst-Planck-Poisson relation was used for solving mass balance, species transport, and electrostatics. The general form for Nernst-Plank is given as

$$N_i = -D_i c_i \frac{1}{RT}\frac{\mathrm{d}\mu_i}{\mathrm{d}x} \quad (14)$$

where D_i is the diffusion coefficient for species i (the D_i values used in this study were tabulated in Table S1), c_i is the local concentration, and μ_i is the electrochemical potential. For the pH 0/pH 14 case, the involved solution species were H_3O^+, OH^-, K^+, and Cl^-. For the pH 7/pH 7 case, the involved solution species were H_3O^+, OH^-, K^+, SO_4^{2-}, and $NaSO_4^-$. For the case with phosphate buffers, the involved solution species were H_3O^+, OH^-, K^+, HPO_4^{2-}, $H_2PO_4^-$, $NaHPO_4^-$, and NaH_2PO_4. For H_3O^+ and OH^-, Eq.15 was used with an additional term accounting for the electric field dependence. For all other mobile species, a common Nernst-Planck Eq.16 was employed. The electrochemical potentials for different species were calculated by

$$\mu_i = \mu_i^0 + RTln\left(\frac{c_i}{c_{H_2O}}\right) + nF\phi - \frac{1}{2}RTln\left(\frac{k_-^E}{k_+^E}\right) \quad (i = H_3O^+, OH^-, c_{WD}H^+, c_{C_{WD}}), \quad (15)$$

$$\mu_i = \mu_i^0 + RTln\left(\frac{c_i}{c_{H_2O}}\right) + nF\phi \quad (i \neq H_3O^+, OH^-), \quad (16)$$

where μ_i^0 is the reference state for species *i* in water at 1 bar, *n* is the charge number for species *i*, ϕ is the electric field, and k_+^E and k_-^E and are the electric field dependent dissociation and recombination rate constants which only applied to H_3O^+ and OH^-. In this model, the electrochemical potentials for hydronium and hydroxide included an explicit dependence on the electric field (Eq. 15). As a result, the transport equation based on (Eq. 14) was modified from the traditional Nernst-Planck relation). Note that for the buffer reactions used in the simulation, such as protonation and deprotonation of phosphate ions, the reaction rate is already at diffusional limit, and further increase of the back and forward reaction rate did not change the simulation results. Combine Eqs. 14, 15, and 16, a general form of species molar flux equation was obtained as the following:

$$N_i = -D_i\frac{dc_i}{dx} + nD_ic_i\frac{FE}{RT} + D_ic_i\frac{dc_{H_2O}}{dx} + 0.5D_ic_i\frac{d\ln\left(\frac{k_-^E}{k_+^E}\right)}{dx} \quad (i = H_3O^+, OH^-). \quad (17)$$

$$N_i = -D_i\frac{dc_i}{dx} + nD_ic_i\frac{FE}{RT} + D_ic_i\frac{dc_{H_2O}}{dx} \quad (i \neq H_3O^+, OH^-), \quad (18)$$

The mass balance was solved using

$$\frac{dN_i}{dx} = R_i \quad (19)$$

where R_i is the reaction mass sources terms due to chemical reactions (R1 to R5). The immobile species, i.e, C_{WD} and $C_{WD}H^+$ were not solved with the Nernst-Planck formulation. The mass balance of C_{WD} and $C_{WD}H^+$ were computed with two additional algebraic equations with a fix

catalyst concentration of 1 M for the reference case. The partition of C_{WD} and $C_{WD}H^+$ was determined by the catalytical reactions R2 and R3:

$$c_{C_{WD}} = \frac{k_2^- c_{OH^-} + k_3^+ c_{H_2O}}{k_2^+ c_{H_2O} + k_2^- c_{OH^-} + k_3^+ c_{H_2O} + k_3^- c_{H_3O^+}} c_{fix} \quad (20)$$

$$c_{C_{WD}H^+} = \frac{k_2^+ c_{H_2O} + k_3^- c_{H_3O^+}}{k_2^+ c_{H_2O} + k_2^- c_{OH^-} + k_3^+ c_{H_2O} + k_3^- c_{H_3O^+}} c_{fix} \quad (21)$$

The Poisson's equation was utilized for solving electrostatics:

$$\frac{d(\varepsilon E)}{dx} = F\sum_i c_i \quad (22)$$

$$-\frac{d\phi}{dx} = E \quad (23)$$

where i is the index for difference species, E is the electrical field, and the ϕ is the electrostatics potential. $c^0_{H_2O}$ in electrolyte is 55.34 M. The c_{H_2O} in the BPM was corrected with its volumetric water fraction ($c_{H_2O} = f_{water} c^0_{H_2O}$, $f_{water} = 0.215$ in this study (experimentally fitted value)). The f_{water} in the membrane was assumed to be a constant value in this study due to small current densities (~ 10 mA cm^{-2}). At high operating current densities, typically > 100 mA cm^{-2}, dehydration of BPM interface limits the attainable water dissociation rates and causes irreversible damage to the BPM interface1 However, at solar flux relevant current densities (tens of mA cm^{-2}), water transport does not pose a limitation as shown in Figure S1. For example, at a current density of ~ 10 mA cm^{-2}, the junction water concentration is only ~1% lower than the case without applied current. Figure S2 shows the effect of f_{water} on the current voltage characteristics of the BPM. We used f_{water} as one of the fitting parameters to fit the experimental BPM current-voltage curves.

The effective diffusion coefficients for each species within the BPM were corrected with Bruggeman model ($D = D^0 f_{\text{water}}{}^{\theta}, \theta = 1.5$).[29] Note that in addition to the mobile species considered in Eqs. 17 and 18, immobile fixed charges within BPM and charged catalytical $C_{WD}H^+$ for the CL was included in Eq. 22. The detailed dielectric constant (ε) as a function of the *x*-position is included in Table S2. Figure S3 illustrates the dielectric constant change across the simulation domain.

The boundary conditions for the Nernst-Planck equations (Eqs.17, 18, and 19) on both sides of the membrane are Dirichlet boundary condition with the concentrations of each spices given as the values in bulk electrolytes. For Poisson equations (Eqs.22 and 23), an electrical ground ($\phi = 0$ V) is considered at $x = 0$ and a constant electrolyte potential is applied at $x = L$. The model was solved numerically using finite element method via Newton method in COMSOL Multiphysics. The relative tolerance was set to be 10^{-4} with a mesh number of 6500. The mesh independent study was conducted to minimize the effect of mesh on the results. A list of governing equations and unknowns was tabulated in table S3. The total number of governing PDEs are 10 for the pH 0/pH 14 case, 12 for the pH 7/pH 7 case, and 16 for the phosphate buffer case. Model parameter including diffusion coefficients and fitting parameters for f_{water} and θ in Bruggeman model (table S1), dielectric constants (table S2), and reaction constants (table S4).

Results and discussion

Figure 1b shows the experimental and modeling comparison of the electrochemical behavior of the BPM at the pH=0/pH=14 electrolyte combination. BPM voltage measurements were performed in a flow electrochemical measurement consisting of a cathode, a catholyte compartment, a BPM, an anolyte compartment and an anode compartment (See Figure S4). The

spacing of the catholyte and the anolyte compartment was 1 cm, and the active area of the cathode, the anode and the BPM was 4 cm^2. The catholyte and the anolyte were fed into the electrochemical cell at a rate of 43 ml min^{-1} using a peristaltic pump. The BPMs used in the experiments are commercial Fumasep bipolar membrane from Fuma-Tech. All the experimental current-voltage measurements were carried out using fresh BPMs that were cut from the same membrane sheet. The BPM voltage was determined by measuring the voltage difference between two Ag/AgCl reference electrodes (1 M KCl, CH instruments), each was placed in the catholyte and the anolyte compartment while applying electrical current to the anode and the cathode using Keithley 2400 in a 4-wire sensing mode.[22,30] The distance between each reference electrode and the BPM was 0.5 cm. The BPM voltage measurements were carried in multistep chronopotentiometry mode from high current density (11 mA cm^{-2}) to low current density (0 mA cm^{-2}). The voltage at each applied current density was recorded once the voltage stabilized to ensure that the BPM voltage was not underestimated. All experimental measurements were carried using fresh BPMs that were cut from the same membrane sheet. Typical transients of the BPM voltages as a function of time at different operating current densities were included in the Figure S5. Note that it can take hundreds of seconds for the solution species and the BPM voltage to reach equilibrium, especially when the operating current density was low (Figure S5). No IR correction was performed in the data presented in this study. The conductivity of infinite diluted K_2SO_4 is 0.0306 S m^2 mol^{-1}.[31] Consider the 0.5 M concentration and 1 cm distance between two reference electrodes, the resistance is estimated as 6.54 Ω. The IR corrected *IV* curve is compared with no IR correction curve in figure S6 for the pH7/7 case.

The vertical dotted line (green) in Figures 1b and 1c indicates the $V_{BPM\_equilibrium}$ = 826 mV at the pH=0/pH=14 electrolyte combination. Different voltages across BPMs at zero operating current

density ranging from 0.74 V to 0.81 V were observed experimentally. The variation of the electrochemical behavior was likely due to different batches of BPMs from commercial vendors. Note that appreciable current densities were observed at voltages less than the $V_{BPM\_equilibrium}$ in all experimental measurements. Co-ion leaking was often accounted for the current densities at voltages less than the $V_{BPM\_equilibrium}$, and WD was not supposed to take place at voltages less than the $V_{BPM\_equilibrium}$.[16] In this case, the co-ion leaking includes the transport of K^+ from the alkaline chamber to the acid chamber, and transport of SO_4^{2-} from the acid chamber to the alkaline chamber.[32] However, the simulated partial current density for WD and co-ion leaking at different voltages across BPM (Figure 1c) showed that significant WD took place at voltages equal or less than the $V_{BPM\_equilibrium.}$ $j_{water\_dissociation}$ is the partial current density due to water dissociation, and j_{coions} is the current density for the coions crossover. For example, at the $V_{BPM\_equilibrium}$ (dashed line in Figure 1c), the WD current density accounted for 77.4% of the total current density, where the co-ion leaking only accounted for 23.6% of the total current density. This phenomenon was not alone at pH=0/pH=14 electrolyte combination. In other pH combinations, significant partial current density related to WD was also observed (See Figure S7) at voltages less than the $V_{BPM\_equilibrium}$. Note that $V_{BPM\_equilibrium}$ in different pH combinations was defined as $V_{BPM_equilibrium} = \Delta$pH x 59 mV, where ΔpH was the pH differential between the two electrolytes [16] , and $V_{BPM\_equilibrium}$ is the thermodynamic voltage that is needed to perform WD reaction in BPM.[3,6,22] In the presence of co-ion leakage, the electrochemical free energy generated by neutralizing the pH gradients between the two sides of the BPM accounted for the voltage shift observed in the simulation. Effectively, a small leaky concentration cell was operating in parallel at low current density to drive the WD at the BPM interface. The relatively small shift in the turn on voltage < 100 mV observed here did not contradict with the thermodynamics of water dissociation within

BPM, but instead additional process, in this case, the co-ion leakage which resulted in gradual neutralization of pHs across the BPM, needs to be considered during the BPM operation, especially at low current densities. As shown in figure 1b and figure S8, as the thickness of the membrane increased and the co-ion leakage decreased, the turn-on potential for water dissociation reaction moved to voltage values closer to $V_{\mathrm{BPM\_equilibrium}}$.

The electrochemical energy dissipated by co-ion leaking at two different pH differentials and effectively neutralizing the pH gradients in the system accounted for the early turn on of the WD reaction. Effectively, a small leaky concentration cell was operating in parallel at low current density to drive the WD at the BPM interface. Effectively, a small leaky concentration cell was operating in parallel at low current density to drive the WD at the BPM interface. For the BPM operated without any co-ions, for example, in a vapor-fed electrolysis system without any liquid/mobile electrolytes, the WD reaction would take place at voltages equal or larger than the $V_{\mathrm{BPM\_equilibrium}}$. Figure 2a shows the experimental and modeling comparison of the electrochemical behavior of the BPM at the pH=7/pH=7 electrolyte combination. The experimental curves and the simulated curves were matched relatively well. The effect of the BPM thickness on the electrochemical behavior is presented in Figure S9. The thinner BPM thickness leads to larger co-ion leakage while smaller ohmic losses. The consideration of ion pairing reaction in the 0.5 M K_2SO_4 electrolyte resulted in a reduced leaking current density at the flat region compared to the case without ion pairing reaction. As shown in Figure S10 the change of the CEL or AEL thickness or the use of asymmetric thicknesses had small effects on the current density-voltage characteristics of the BPM, mainly because the resistive loss across the CEM or AEM was small at low operating current densities. The reduced leaking current density due to the reduced concentration of mobile ions was a better match to the experimental results. Figure 2b shows the

simulated partial current density for WD and co-ion leaking as a function of the applied potential with or without the consideration of ion paring. Two distinctive regions, one relatively flat region at voltage < 0.6 V, and one exponential turn-on region at voltage > 0.6 V, were observed, which corresponds to co-ion leaking and WD reaction at BPM interface, respectively. The total concentration as well as the size of the mobile ions due to ion pairing changed the co-ion leaking current density significantly. The flat region shows a limited current density with increasing applied voltage due to limited water dissociation rate at the CL with only leaking current from co-ions movement through the BPM (Figure 2b). The co-ion leaking current density was found to be ~ 1 mA cm^{-2} in this study and this value can reach ~ 2 mA cm^{-2} if ion pairing effect is neglected. The membrane/electrolyte interface was modeled and simulated to understand the transport and junction profile across the interface as illustrated in Figure 2c. The selected case is the pH 7-7 with an operating current density of 3 mA cm^{-2}. The net charge (dark blue curve) from both mobile ions and fixed ions in the system accounted for the abrupt potential change (dotted brown curve) across the BPM/electrolyte interface. Noted that the width of the space charge region within CEM at the operating current density of 3 mA cm^{-2} was ~3 nm from the simulation, and the width of the double layer in the aqueous electrolyte was typically smaller than 50 nm, both of which agreed with literature values. At different applied voltage across the BPM, the contribution of catalyzed pathway and uncatalyzed pathway of WD was simulated in Figure 2d. WD from un-catalyzed pathway (Eq. 1, black curve) played the major role in V_{BPM} > 0.6 V during the operation. Because the intrinsic forward reaction rate of the catalyzed pathway was larger than the un-catalyzed pathway and both reactions had the same electric-field dependence, the WD rates from catalyzed pathway dominated at small membrane voltages. At higher membrane voltages, the protonation and deprotonation of the WD catalyst (Eqs. 7 and 9) became the rate determining step, which

significantly constrained the overall WD in the catalyzed pathway. As shown in Figure 2d, the catalyzed pathway exhibited a sigmoidal behavior, where the reaction rate remained relatively unchanged between 0 to 0.2 V and between 0.6 V to 1 V. The electric field enhancement for R2 was minimum at voltage smaller than ~0.2 V, and the high rate constants at zero field for the catalyzed pathway (i.e., k^0_{+2} and k^0_{-2}) accounted for the flat region between 0 to 0.2 V. As the voltage increased beyond 0.6 V, the electric field independent R3 became the rate limiting step, which accounted for the flat region between 0.6 V to 1 V. To improve the electrochemical behavior of BPMs, in particular, in operating current densities relevant to areal-matched solar fluxes, several simulated strategies were applied to show the impact on the turn-on potential of the BPMs. Figure 3a shows the simulated total current density as a function of the BPM voltage with different pKa of the WD catalyst. To operate at 10 mA cm^{-2}, the voltage across the BPMs decreased from 0.875 V to 0.29 V when the pKa of the WD catalyst decreased from 12.08 to 6.08.

While the electrochemical behavior of the BPMs showed dramatic difference at different pKa of WD catalysts, the concentration profile of H^+, OH^- and other co-ions across the BPM remained the same as illustrated in Figure 3b at the same operating current density. The concentrations of each species are quite flat at two boundary layers. The low H^+ concentration is mainly due to the low operating current density at 3 mA cm^{-2}, as the H^+ concentration is dependent on the current density, the H^+ peak concentration increased from 0.022 M to 0.4 M when increase the current density from 3 mA cm^{-2} to 40 mA cm^{-2} (Figure S11). A logarithm concentration profile for 3 mA cm^{-2} is also shown in Figure S12. Figure 3c shows the net charge density, the charge density of the WD catalyst, and the junction potential across the CL within BPM at 3 mA cm^{-2} with two different pKa values of the WD catalysts. The decrease of the net charge density (black curve) within BPM interface accounted for the decrease of the potential change with WD catalyst at a low pKa value.

The net charge density difference between two cases was attributed to higher $C_{WD}H^+$ charge density at higher R3 forward reaction rate. A space chare region of ~3 nm can be also seen from figure 3c. As shown in Figure 3d, by decreasing the pKa value of the WD catalyst, the catalyzed pathway (dotted red curve) was enhanced significantly and became the dominating contribution to the total current density. For example, at V_{BPM} = 0.8 V, the catalyst pathway for non-enhanced case was only 2.76 mol m^{-3} s^{-1} and increased to 11.86 mol m^{-3} s^{-1} when enhanced by 10^4. A detailed schematic showing the two-pathway water dissociation is presented in Figure S13.

Figure 4a shows the impact of the enhancement of the field dependent WD rate, k^0_{+2}, in the catalyzed pathway. A relatively small change in the turn-on potential was observed when the enhancement factor for $k^0_{+2}$was parametrically swept from 1 to 10000. As shown in Figure 4b, the fixed charge density due to the WD catalyst exhibited a very different profile within the BPM junction layer, which gave rise to the potential profile. As noted previously, the protonation and deprotonation of the WD catalyst (Eqs. 7 and 9) was the rate determining step for WD, as a result, enhancing k^0_{+2} does not increase the contribution from the catalyzed pathway as shown in Figure 4c. However, the change of the potential gradient between 0 nm to ~1.5 nm within the junction was enhanced by the change of k^0_{+2}, which improved the turn on for the un-catalyzed WD pathway.

Furthermore, the impact of the width of the junction as well as the fixed charge density of BPM on the electrochemical behavior of BPM was modeled and simulated. Figure 5 shows the effects of the width of the CL and the fixed charge density in BPM. When the CL thickness was varied from 5 nm to 100 nm, the current voltage characteristic of BPM remained unchanged. As shown in Figure 5b, the net charge density and the potential profile in CL was almost identical in two different CL thicknesses. The majority of the electric field enhancement and the associated WD reactions took place within the first few nanometers in the CL, and as a result, the increase of the

CL thickness played a very minimal role in electrochemical behavior of BPM. In contrast, when the fixed charge in BPM was increased from 0.5 M to 2.5 M, noticeable difference in the current voltage characteristic of BPM was observed (Figure 5c). The voltage across BPM decreased from 1.21 V to 0.67 V at an operating current density of 10 mA cm^{-2} when the fixed charge in BPM increased from 0.5 M to 2.5 M. The water dissociation turn on voltage also reduced from ~0.7 V to ~0.5 V with increased fix charge density from 0.5 M to 2.5 M due to increased net charge density generated at the CL layer at increased fix charge density (see Figure S14). In addition, the increase of the fixed charge in BPM also decreased the co-ion leaking between the cathode and anode chamber. The co-ion leaking current density decreased from 1.78 mA cm^{-2} to 0.9 mA cm^{-2} when the fixed charge in BPM increased from 0.5 M to 2.5 M. This was a result of the reduced migration of co-ion (K^+) due to decreased mobile cations within the CEL (see figure S15) with the increasing fix charge density.

Figure 6a shows the experimental and modeling comparison of the electrochemical behavior of the BPM using buffered electrolyte at the pH=7/pH=7 electrolyte combination. To fit the experimental curve (only for the buffer case), the exponential factor, θ, in the Bruggeman model for K^+, $H_2PO_4^-$ and HPO_4^{2-} were set to 2.1, 1.0 and 1.0, respectively, and f_{water} was set to 0.158. The change of fitting is used accounting for relative diffusion coefficient with the present of phosphate ions. The interaction between the buffer ions and polymer membranes with fixed charges can significantly alter the effective diffusion coefficient of solution species within the BPM. In contrast with the un-buffered electrolyte (Figure 2a), two distinctive plateaus of current densities, one between 0 to ~250 mV, and one between ~400 mV to ~500 mV (see Figure 6a), were observed reproducibly in the steady-state measurements. At 0 to 250 mV, the major current carrier was the K^+ leaking (Figure 6b), for instance, the K^+ leaking accounted for ~60.6% of the

total current at 0.2 V. Two other major partial current densities were carried by HPO_4^{2-} and $H_2PO_4^-$ accounting for 26.2% and 12.7%. While H^+ only carried ~0.5% of the total current density, indicating limited water dissociation rate in this regime. The further increase in current density in range of ~250 mV to ~500 mV attributed to the increase H^+ generation from the buffer reaction, as shown in Fig. 6b. As the current density continued to increase, significant pH gradients were observed within the BPM (Figure 6c), the buffer species were fully deprotonated at the high pH condition in the catalyst layer, and as a result, a significant decrease of the proton current density from the buffered reaction was observed ~600 mV. Further exponential increase in current density with the increasing voltage after ~650 mV was accounted by the WD reaction due to the large electrical gradients. Two distinctive pH profiles were observed between the buffered case and un-buffered case, as shown in figure 6c. At three different operating current densities, the buffered electrolyte was able to maintain the pH relatively constant within the BLs, while the majority of the pH drop took place within the AEM or CEM layers. In contrast, in the un-buffered electrolyte, relatively small change of pHs was observed within the AEM or CEM layers, and significant pH drops took place within the BLs. Note that the pH values at the BPM interfaces were almost identical between the buffered or non-buffered cases. The pH gradients across the simulation domain in both the buffered electrolyte and un-buffered electrolyte accounted for very small voltage drops during the operation, the majority of the voltage drops took place within the CL. However, in solar-fuel devices, the detailed pH profiles would be an important factor for the placement of electrocatalysts to minimize the Nernstian potential loss and to optimize the activity and selectivity of the catalyst under specific pH conditions.

Summary

In summary, the 1D Multiphysics model that accounts for WD kinetics and species transport in BPM successfully predicted the electrochemical behavior of BPM under solar flux relevant current densities in various electrolyte, buffered or unbuffered, combinations. Significant partial current densities for WD were observed at BPM voltages much less than the equilibrium voltage, e.g., $59\ \mathrm{mV} \times \Delta\mathrm{pH}$ from both from experiments and from the modeling. The co-ion leaking across the BPM at pH differentials accounted for the early presence of the partial current density for WD. Two distinctive electric field dependent WD pathways, the un-catalyzed pathway and the catalyzed pathway, were simulated quantitatively and parametrically studied to improve the turn-on potential of the BPM. The catalyzed pathway accounted for the majority of the partial current density for WD at low voltages, while the un-catalyzed pathway dominated the WD at relatively high voltages. By lowering the pKa of the WD catalysts and improving the rate limiting step in the catalyzed pathway, e.g., the deprotonation step associated with WD catalyst, significant improvement in the turn-on potential was observed. For example, by lowing the pKa of the WD catalysts from 12.08 to 4.08, the voltage required to operate at 10 mA cm^{-2} lowered from 875 mV to 290 mV. Improvements in the turn-on potentials were also observed when the electric field dependent WD rate, K_2, in the catalyzed pathway was enhanced. The increase of the electric field strength at the interfacial CL, which enhanced the un-catalyzed pathway, accounted for the turn-on potential improvements. The width of the CL exhibited minimal effects on the BPM current voltage behavior since the majority of the net charge density and the rapid change of the potential profile took place within the first few nanometer in the CL. The increase of the fixed charge density in BPM improved the turn-on potential and at the same time decreased the co-ion leaking at low voltage regions. The two plateau, titration-like behavior in the current voltage characteristics with buffered electrolyte was observed experimentally under steady state conditions. In the buffered

electrolyte, the majority of the pH drops took place within the CEM and AEM, while in the un-buffered electrolyte, the majority of the pH drops took place at the aqueous electrolyte layer. The voltage penalty associated with WD, even at relatively low operating current density, accounted for the majority of the voltage loss in BPM system. Development and implementation of WD catalysts with optimal pKa under operation conditions as well as fundamental understanding of the electric field dependent water dissociation constant can guide and improve the electrochemical behavior of the BPM systems.

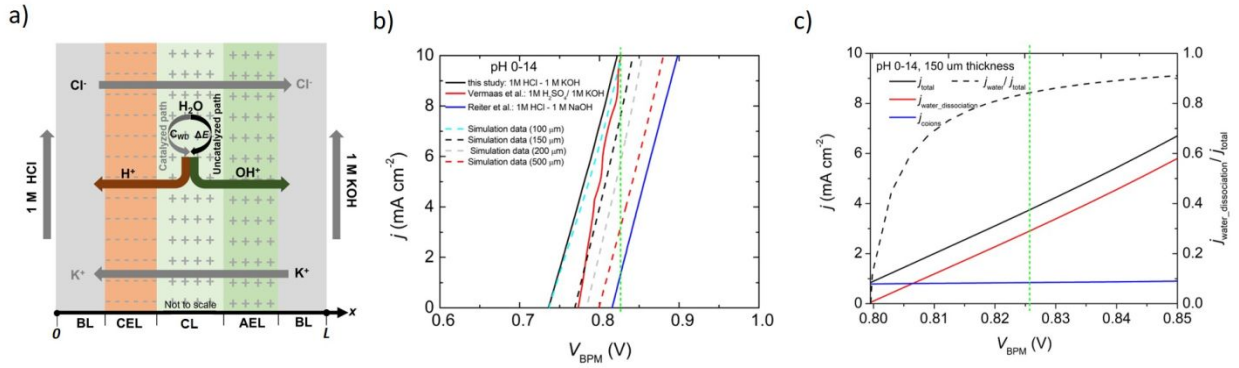

Figure 1. (a) A schematic illustration of the modeling domain in bipolar membrane. (b) The experimental and modeling comparison of the electrochemical behavior of the BPM at the pH=0/pH=14 electrolyte combination. Four membrane thickness (100, 150, 200, and 500 μm) are shown in dashed lines. (c) The simulated partial current density for WD and co-ion leaking as a function of the voltage across the BPM. $j_{\text{water\_dissociation}}$ is the partial current density due to water dissociation, and j_{coions} is for coions crossover. The vertical dotted line (green) indicates the $V_{\text{BPM\_equilibrium}}$ = 826 mV at the pH=0/pH=14 electrolyte combination.

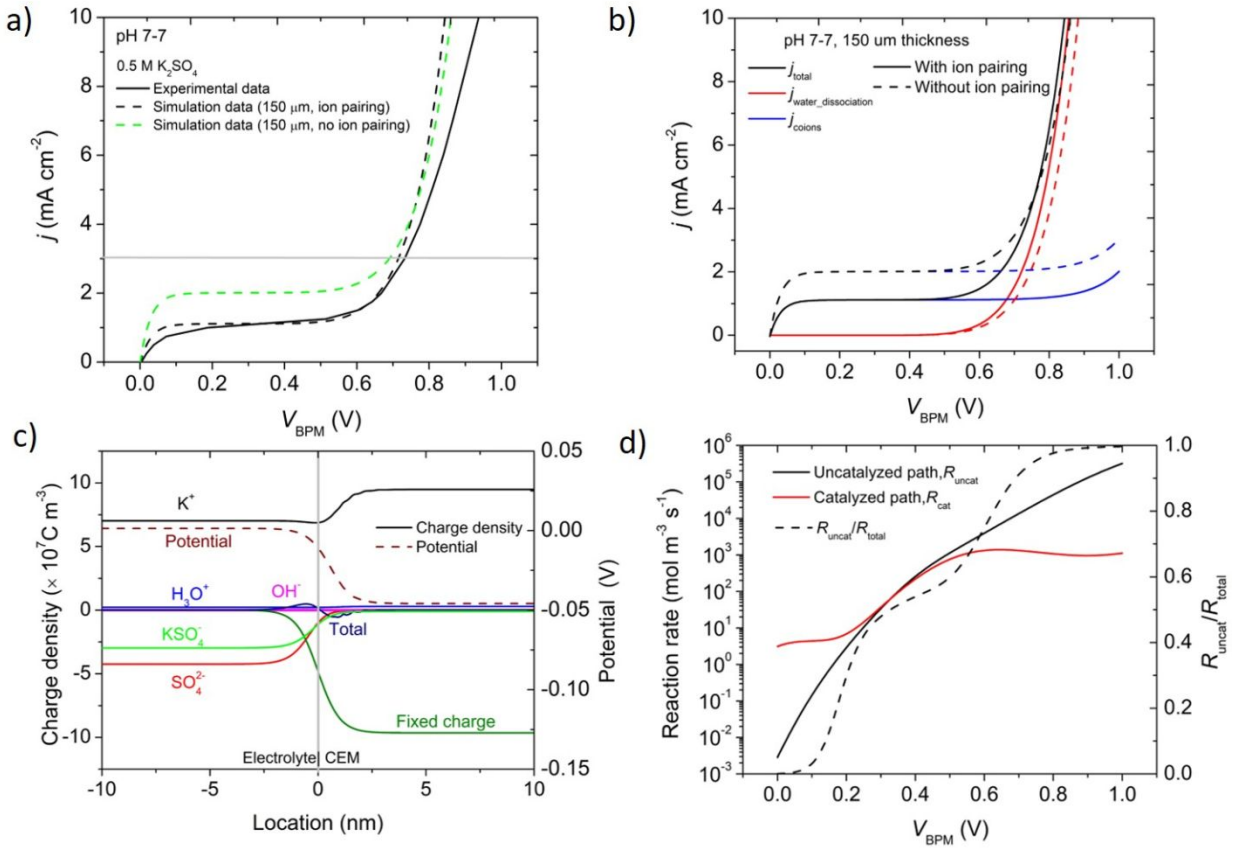

Figure 2. (a) The experimental and modeling comparison of the electrochemical behavior of the BPM at the pH=7/pH=7 electrolyte combination, i.e 0.5 M K_2SO_4. (b) The simulated partial current density for WD and co-ion leaking as a function of the applied potential with or without the consideration of ion paring using 0.5 M K_2SO_4 electrolyte . (c) The charge density of various species and the potential across the membrane/electrolyte interface at current density of 3 mA cm^{-2}. (d) The simulated contribution of catalyzed pathway and uncatalyzed pathway of WD as a function of voltage across the BPM.

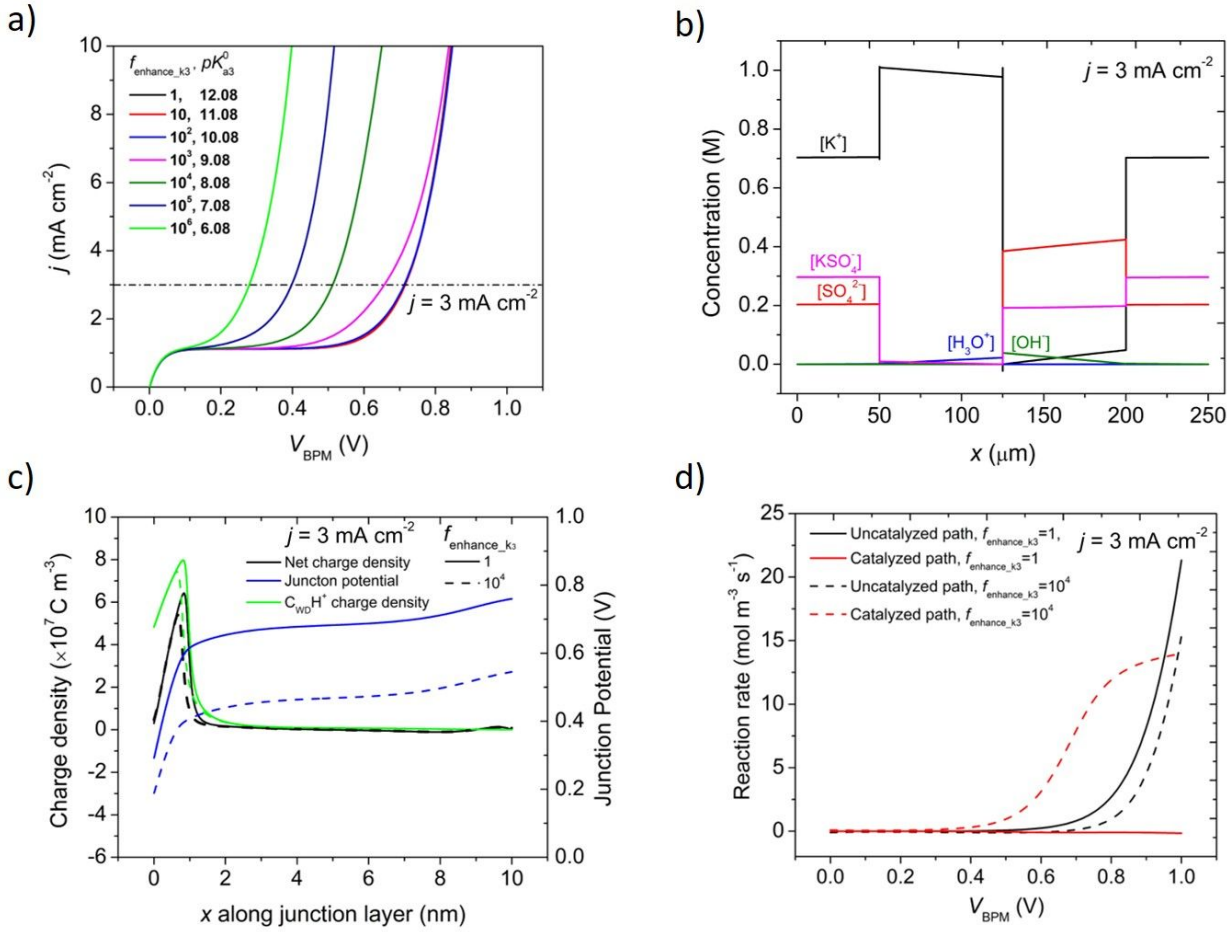

Figure 3. Improving the turn-on potential of BPM by optimizing the pKa of the immobilized WD catalyst. (a) The simulated total current density as a function of the BPM voltage with different pKa of the WD catalyst. (b) The concentration profile of H_3O^+, OH^- and other co-ions across the BPM at different pKa of the WD catalyst at a current density of 3 mA cm^{-2}. (c) The net charge density, the charge density of the WD catalyst, and the junction potential across the CL within BPM at 3 mA cm^{-2} with two different pKa of the WD catalysts. (d) The simulated contribution of catalyzed pathway and uncatalyzed pathway of WD as a function of voltage across the BPM with two different pKa of the WD catalysts at a current density of 3 mA cm^{-2}.

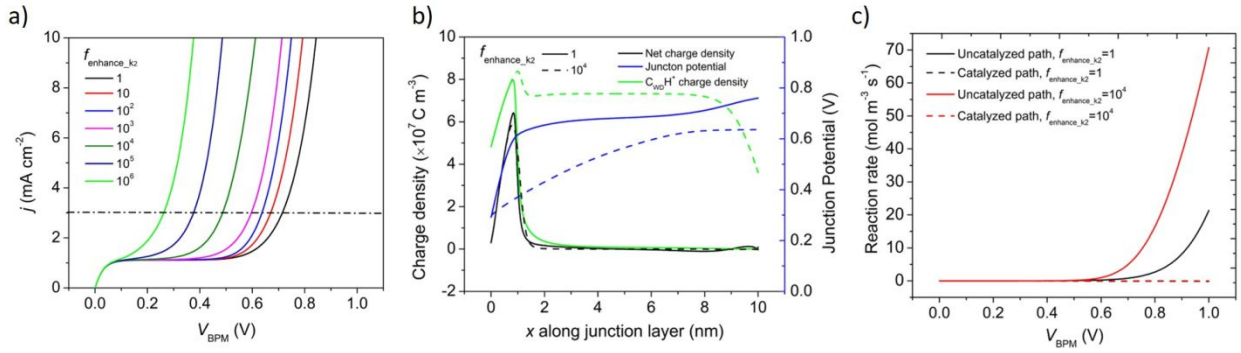

Figure 4. Improving the turn-on potential of BPM by improving the electric field dependent WD rate, k_{+2}, in the catalyzed pathway. The electrolytes on both sides of BPM are 0.5 M K_2SO_4 .(a) The simulated total current density as a function of the BPM voltage with different enhancement factor of k_{+2} ($f_{enhance\_k2}$). (b) The net charge density, the charge density of the WD catalyst, and the junction potential across the CL within BPM at 3 mA cm^{-2} with two different $f_{enhance\_k2}$. (c) The simulated contribution of catalyzed pathway and uncatalyzed pathway of WD as a function of BPM voltage with two different $f_{enhance\_k2}$.

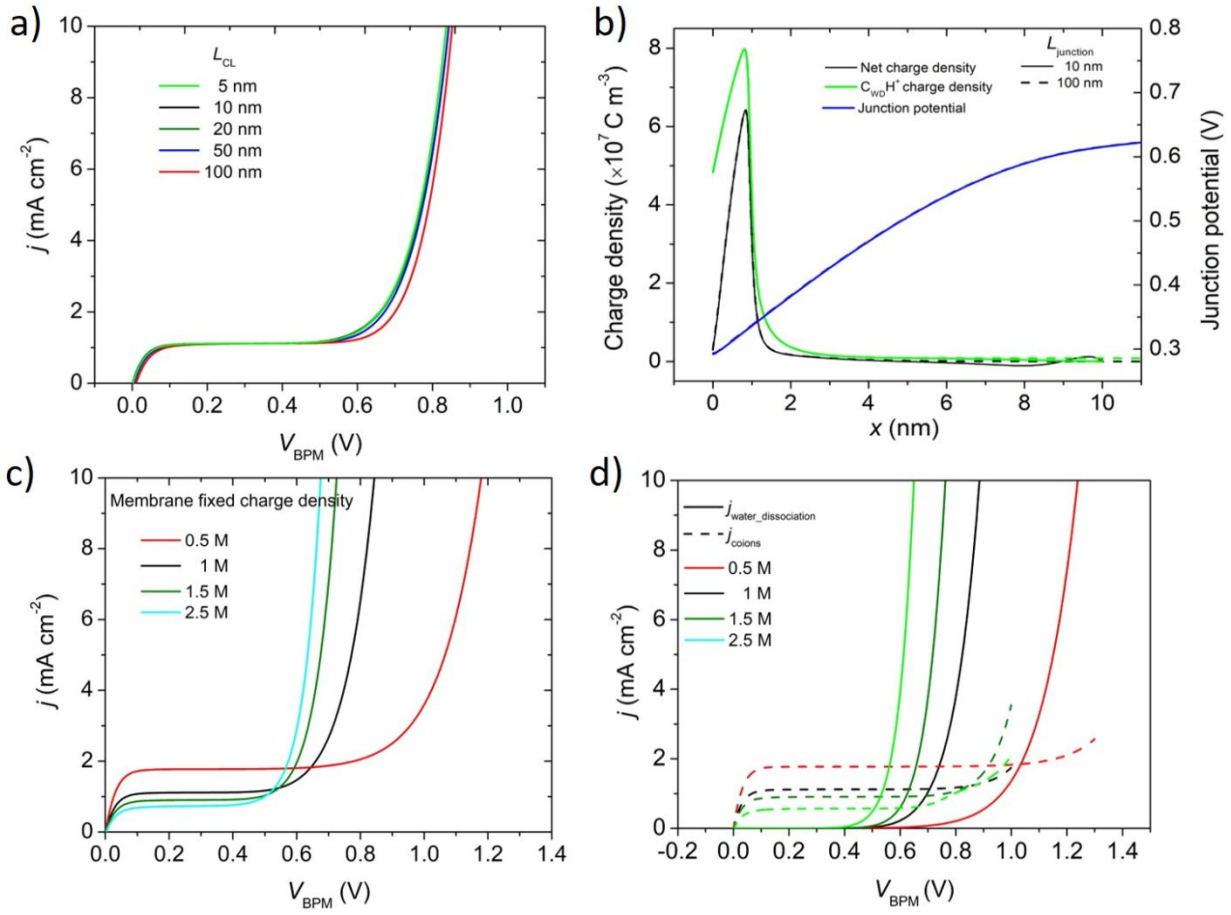

Figure 5. Improving the turn-on potential of BPM by improving the width of the CL and the fixed charge density in BPM. The electrolytes on both sides of BPM are 0.5 M K_2SO_4 . (a) The simulated total current density as a function of the BPM voltage with different widths of the CL. (b) The simulated net charge density, the charge density of the WD catalyst, and the junction potential across the CL within BPM at two different widths of the CL. (c) The simulated total current density as a function of the BPM voltage with different fixed charge densities in AEM and CEM. (d) The simulated partial current density for WD and co-ion leaking as a function of the BPM voltage at different fixed charge densities in AEM and CEM.

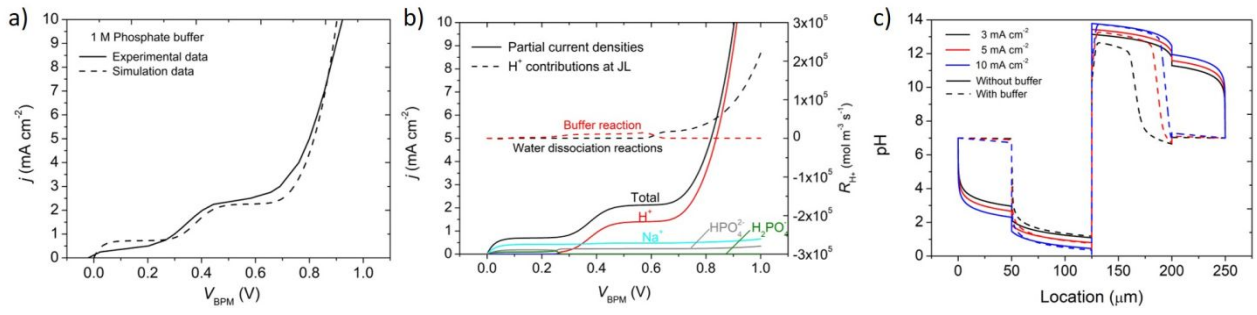

Figure 6. Modeling electrochemical behavior of BPM in buffered electrolytes (a) The experimental and modeling comparison of the electrochemical behavior of the BPM at the pH=7/pH=7 combination with 1M buffered electrolytes. (b) Partial current densities of different charged species for the buffer case and CL H^+ generation rates differentiating the contribution of buffer reaction and water dissociation reactions (b) The pH profile along the BPM for the cases without buffer (solid lines) and with buffer (dash lines) at 3, 5, 10 mA cm^{-2}.

Acknowledgement

This material is based on work performed by the Liquid Sunlight Alliance, which is supported by the U.S. Department of Energy, Office of Science, Office of Basic Energy Sciences, Fuels from Sunlight Hub under Award Number DE-SC0021266. Meng Lin acknowledges support from the Swiss National Science Foundation through the Early Postdoc Mobility Fellowship, grant no. P2ELP2_178290 and Centers for Mechanical Engineering Research and Education at MIT and SUSTech.

References:

1 J. Luo, D. A. Vermaas, D. Bi, A. Hagfeldt, W. A. Smith and M. Grätzel, *Adv. Energy Mater.*, , DOI:10.1002/aenm.201600100.

2 D. A. Vermaas, M. Sassenburg and W. A. Smith, *J. Mater. Chem. A*, 2015, **3**, 19556–19562.

3 X. Zhou, R. Liu, K. Sun, Y. Chen, E. Verlage, S. A. Francis, N. S. Lewis and C. Xiang, *ACS Energy Lett.*, 2016, **1**, 764–770.

4 Y. Wang, J. Liu, Y. Wang, Y. Wang and G. Zheng, *Nat. Commun.*, , DOI:10.1038/s41467-018-07380-x.

5 Y. C. Li, D. Zhou, Z. Yan, R. H. Gonçalves, D. A. Salvatore, C. P. Berlinguette and T. E. Mallouk, *ACS Energy Lett.*, 2016, **1**, 1149–1153.

6 K. Sun, R. Liu, Y. Chen, E. Verlage, N. S. Lewis and C. Xiang, *Adv. Energy Mater.*

7 M. Lin, L. Han, M. R. Singh and C. Xiang, *ACS Appl. Energy Mater.*, 2019, **2**, 5843–5850.

8 A. Pătru, T. Binninger, B. Pribyl and T. J. Schmidt, *J. Electrochem. Soc.*, 2019, **166**, F34–F43.

9 Y. C. Li, G. Lee, T. Yuan, Y. Wang, D. H. Nam, Z. Wang, F. P. Garciá De Arquer, Y. Lum, C. T. Dinh, O. Voznyy and E. H. Sargent, *ACS Energy Lett.*, 2019, **4**, 1427–1431.

10 T. Li, E. W. Lees, M. Goldman, D. A. Salvatore, D. M. Weekes and C. P. Berlinguette, *Joule*, 2019, **3**, 1487–1497.

11 J. R. Davis, Y. Chen, J. C. Baygents and J. Farrell, *ACS Sustain. Chem. Eng.*, , DOI:10.1021/acssuschemeng.5b00654.

12 X. Tongwen, *Resour. Conserv. Recycl.*, , DOI:10.1016/S0921-3449(02)00032-0.

13 C. Huang and T. Xu, *Environ. Sci. Technol.*, 2006.

14 M. R. Singh, E. L. Clark and A. T. Bell, *Phys. Chem. Chem. Phys.*, 2015, **17**, 18924–18936.

15 Y. Chen, N. S. Lewis and C. Xiang, *ACS Energy Lett.*, 2016, **1**, 273–280.

16 D. A. Vermaas, S. Wiegman, T. Nagaki and W. A. Smith, *Sustain. Energy Fuels*, 2018, **2**, 2006–2015.

17 M. A. Blommaert, D. A. Vermaas, B. Izelaar, B. in ’t Veen and W. A. Smith, *J. Mater. Chem. A*, 2019, 19060–19069.

18 S. Z. Oener, S. Ardo and S. W. Boettcher, *ACS Energy Lett.*, 2017, **2**, 2625–2634.

19 L. Onsager, *J. Chem. Phys.*, 1934, **2**, 599–615.

20 H. Strathmann, J. J. Krol, H. J. Rapp and G. Eigenberger, *J. Memb. Sci.*, 1997, **125**, 123–142.

21 S. A. Mareev, E. Evdochenko, M. Wessling, O. A. Kozaderova, S. I. Niftaliev, N. D. Pismenskaya and V. V. Nikonenko, *J. Memb. Sci.*, 2020, **603**, 118010.

22 S. Z. Oener, M. J. Foster and S. W. Boettcher, *Science*, , DOI:10.1126/science.aaz1487.

23 L. Onsager and R. M. Fuoss, *J. Phys. Chem.*, 1932, **36**, 2689–2778.

24 N. Craig, *UC Berkeley Electron. Theses Diss.*, 2013, 116.

25 K. N. Grew, J. P. McClure, D. Chu, P. A. Kohl and J. M. Ahlfield, *J. Electrochem. Soc.*, 2016, **163**, F1572–F1587.

26 A. A. Green, *J. Am. Chem. Soc.*, 1933, **55**, 2331–2336.

27 E. J. Reardon, *J. Phys. Chem.*, 1975, **79**, 422–425.

28 J. J. Krol, M. Jansink, M. Wessling and H. Strathmann, *Sep. Purif. Technol.*, 1998, **14**, 41–52.

29 P. K. Das, X. Li and Z. S. Liu, *Appl. Energy*, 2010, 87, 2785–2796.

30 D. A. Vermaas, S. Wiegman, T. Nagaki and W. A. Smith, *Sustain. Energy Fuels*, 2018, **2**, 2006–2015.

31 P. Atkins and J. De Paula, in *Physical Chemistry*, 2010.

32 Z. Yan, L. Zhu, Y. C. Li, R. J. Wycisk, P. N. Pintauro, M. A. Hickner and T. E. Mallouk, *Energy Environ. Sci.*, , DOI:10.1039/c8ee01192c.

33 D. Bohra, J. H. Chaudhry, T. Burdyny, E. A. Pidko and W. A. Smith, *Energy Environ. Sci.*, 2019, **12**, 3380–3389.